Nano Res. 2011, 4(1): 61–71
DOI 10.1007/s12274-010-0042-4
ISSN 1998-0124
CN 11-5974/O4
Research Article

Catalytic Properties of Pt Cluster-Decorated CeO_2 Nanostructures

Lin Feng[1,2], Dat Tien Hoang[1], Chia-Kuang Tsung[1,3], Wenyu Huang[1], Sylvia Hsiao-Yun Lo[1], Jennifer B. Wood[1], Hungta Wang[1], Jinyao Tang[1], and Peidong Yang[1] (✉)

[1] Department of Chemistry, University of California, Berkeley, California 94720, USA
[2] Department of Chemistry, Tsinghua University, Beijing 100084, China
[3] Department of Chemistry, Merkert Chemistry Center, Boston College, 2609 Beacon Street, Chestnut Hill, Massachusetts 02467, USA

Received: 24 August 2010 / Revised: 9 September 2010 / Accepted: 9 September 2010

ABSTRACT

Uniform clusters of Pt have been deposited on the surface of capping-agent-free CeO_2 nanooctahedra and nanorods using electron beam (e-beam) evaporation. The coverage of the Pt nanocluster layer can be controlled by adjusting the e-beam evaporation time. The resulting e-beam evaporated Pt nanocluster layers on the CeO_2 surfaces have a clean surface and clean interface between Pt and CeO_2. Different growth behaviors of Pt on the two types of CeO_2 nanocrystals were observed, with epitaxial growth of Pt on CeO_2 nanooctahedra and random growth of Pt on CeO_2 nanorods. The structures of the Pt clusters on the two different types of CeO_2 nanocrystals have been studied and compared by using them as catalysts for model reactions. The results of hydrogenation reactions clearly showed the clean and similar chemical surface of the Pt clusters in both catalysts. The support-dependent activity of these catalysts was demonstrated by CO oxidation. The Pt/CeO_2 nanorods showed much higher activity compared with Pt/CeO_2 nanooctahedra because of the higher concentration of oxygen vacancies in the CeO_2 nanorods. The structure-dependent selectivity of dehydrogenation reactions indicates that the structures of the Pt on CeO_2 nanorods and nanooctahedra are different. Thes differences arise because the metal deposition behaviors are modulated by the strong metal–metal oxide interactions.

KEYWORDS

Nanocrystals, nanoclusters, interface, catalysis

1. Introduction

Metal nanoparticles and metal oxide supports are two major components of most heterogeneous catalysts [1–4]. It is well known that catalytic activity and selectivity are highly dependent on the type of metal oxide support used [5–7], and catalysis can be modulated by using different metal oxide supports [8]. A great deal of research has been devoted to understanding the interaction between metals and different metal oxide supports in order to design better catalysts [9–12]. Recently, cerium oxide (CeO_2) has become a very attractive candidate as a metal oxide support [13–15]. CeO_2 has extensively documented oxygen storage capacity (OSC) [16–18] and results in strong metal–metal oxide interactions [19]. Due to these unique properties, metal/CeO_2 catalysts show great activity for reactions such hydrogenation, the water gas shift, and CO and hydrocarbon oxidation [20–22]. Most previous studies have focused on traditional

---

Address correspondence to p_yang@berkeley.edu

supported metal catalysts, which are prepared by depositing metal clusters on the surface of micron-size CeO_2 supports. However, in these studies the size, shape, and crystal structure of the CeO_2 supports were not controlled at the nanoscale [23–25]. Less attention has been paid to the effects of the nanostructure of CeO_2 supports. Flytzani-Stephanopoulos et al. reported one of the few catalytic studies using different nanostructured CeO_2 materials, employing them as a support to deposit gold clusters [26]. The resulting Au/CeO_2 catalysts showed a strong support-shape effect in the water gas shift reaction. Further studies of the deposition of different metal clusters on nanostructured CeO_2 are merited because of two consequences of the strong metal–metal oxide interaction: The interaction potentially changes the intrinsic properties of the metal and metal oxide, and moreover, is strong enough to affect metal growth behavior on deposition. Further study of deposition methods would also be useful in understanding this phenomenon.

Electron beam (e-beam) evaporation is a frequently used method for the preparation of overgrowth thin films or thin cluster layers on substrates. It is popular because of its conceptual and experimental simplicity; the source material is transformed into its gaseous state, which is then condensed on the substrate. The clean surface and chemical purity of the resulting evaporated cluster layer make it ideal for the synthesis of model catalysts. Herein, we describe the use of the e-beam evaporation method and shape controlled metal oxide nanostructures to synthesize model catalysts. In this instance, shape-specific CeO_2 nanocrystals were first synthesized and subsequently decorated with a thin Pt cluster layer. The as-synthesized CeO_2 nanocrystals have no organic capping. The structure of the composite nanomaterials was analyzed by electron microscopy. The nanosupport-dependent catalytic behaviors were demonstrated by model hydrogenation, dehydrogenation, and oxidation reactions. The information gained from this study will lead to a better understanding of the interactions between metals and metal oxides.

2. Methods

2.1 Characterization methods and instrumentation

Powder X-ray diffraction (XRD) patterns were recorded with a GADDS Hi-Star D8 diffractometer (Bruker) using Co $K\alpha$ radiation ($\lambda = 1.790$ Å). XRD samples were prepared by depositing the precipitated samples on a silicon plate. The sizes and morphologies of the as-obtained nanocrystals were examined with a FEI Tecnai G2 S-Twin transmission electron microscope at an accelerating voltage of 200 kV and a field emission scanning electron microscope (FESEM, JEOL6430) with an operating voltage of 5 kV. The samples were prepared by casting the dilute colloidal solution onto carbon-coated copper transmission electron microscopy (TEM) grids and silicon wafers, respectively. X-ray photoelectron spectroscopy (XPS) experiments were performed on a Perkin–Elmer PHI 5300 XPS spectrometer with a position-sensitive detector and a hemispherical energy analyzer in an ion-pumped chamber (evacuated to 2×10^{-9} Torr). The Al $K\alpha$ ($h\nu = 1486.6$ eV) X-ray source was operated at 300 W with 15 kV acceleration voltage. Binding energies (BE) were calibrated by setting the measured BE of C 1s to 285 eV.

2.2 Synthesis of CeO_2 nanorods and nanooctahedra

The uniform organic-capping-free CeO_2 nanostructures were synthesized in two morphologies, rod-like and octahedral, by using a hydrothermal process [27]. $Ce(NO_3)_3{\cdot}6H_2O$ was used as the cerium source., No organic surfactant or template was introduced in the synthesis. For CeO_2 nanooctahedra, 434.3 mg of $Ce(NO_3)_3{\cdot}6H_2O$ and 1.6 mg of Na_3PO_4 were mixed in 40 mL of D.I. H_2O and sonicated for 30 min. The mixed solution with of pH 4 was then transferred into the Teflon-liner of a hydrothermal autoclave. The autoclave was heated to 170 °C for 12 h. The as-synthesized CeO_2 nanooctahedra were collected and cleaned by centrifugation at 10,000 r/min for 5 min and re-dispersed twice in ethanol. The supernatant was discarded and the precipitated product was then calcined at 400 °C for 4 h. The CeO_2 nanorods were synthesized by adjusting the pH value of the precursor solution from 4 to 2 with dilute hydrochloric acid solution and employing the same hydrothermal treatment. For the synthesis of the CeO_2 nanorods, the pH value is very crucial and needs to be very precise.

2.3 E-beam evaporation of Pt

A homogeneous thick layer of CeO_2 nanostructures was drop casted on a 1.8 × 0.9 cm silicon wafer. After Ar plasma treatment for few seconds, a low density Pt nanocluster layer was deposited by an e-beam evaporator with a background pressure of ~2×10^{-6} Torr. The Pt evaporation rate and deposition thickness were monitored by a crystal monitor. The evaporation rate is controlled by the electron beam current and was fixed at 0.01 nm/s. Different amounts of Pt were deposited by varying the evaporation time.

2.4 Ethylene hydrogenation and cyclohexene hydrogenation/dehydrogenation

Catalytic activities of CeO_2 nanooctahedra and nanorods with the same amount of deposited Pt were measured and compared. For catalytic studies, samples were loaded into glass reactors. Temperature was controlled by a proportional–integral–derivative (PID) controller (Watlow 96) and a type-K thermocouple. Gases were all ultrahigh-purity (UHP) from Praxair. Gas flows were regulated using calibrated mass flow controllers. Before the reaction, samples were reduced in 50 $mL \cdot min^{-1}$ of 76 Torr of H_2 with a He balance for 1 h at 100 °C. For ethylene hydrogenation, the gas mixture was composed of 10 Torr of ethylene and 100 Torr of H_2 with a balance of He. For cyclohexene hydrogenation/dehydrogenation, the feed was 10 Torr of C_6H_{10} (Sigma–Aldrich) and 200 Torr of H_2 with a balance of He. The desired partial pressure of C_6H_{10} was achieved by bubbling He through C_6H_{10} and assuming saturation. All lines before and after the quartz U-tube reactor were heated to 393 K to prevent condensation of organic compounds.

2.5 CO oxidation

The CO oxidation reaction was also used to evaluate the catalytic properties of Pt/CeO_2 nanooctahedra and nanorods. CO oxidation reactions were carried out in a laboratory scale reactor with gas recirculation. The reaction temperature was between 170 and 230 °C. Samples were loaded into quartz reactors and the reaction temperature was recorded by a type-K thermocouple placed near the sample. Prior to the reaction, the reactor was filled with 40 Torr of CO, 100 Torr of O_2, and 620 Torr of He. Gas composition was analyzed with a HP 5890 Series II gas chromatograph equipped with a thermal conductivity (TCD) detector. Turnover frequency (TOF) was calculated by extrapolating the conversion data to the initial time. The numbers of available Pt active sites on the catalysts were calculated from the TEM and ethylene hydrogenation reaction.

3. Results and discussion

3.1 CeO_2 nanorods and nanooctahedra without organic capping agents

The structures of as-synthesized CeO_2 nanooctahedra and nanorods were confirmed by Scanning electron microscope (SEM) and TEM (Fig. 1). Even without organic capping agents, CeO_2 nanostructures were well-dispersed and no aggregation of nanocrystals was observed under SEM imaging. Furthermore, well-defined morphologies can easily be obtained by simply adjusting the pH value of the precursor. The TEM images show that both CeO_2 octahedra and rods have high uniformity and well-defined morphologies (Figs. 1(c) and 1(d)). The edge length of the octahedra is ~100 nm. The widths of the CeO_2 nanorods are ~20 nm and the lengths are around several hundred nanometers. The crystal structures of the CeO_2 nanostructures were confirmed by XRD (Fig. 2). The diffraction peaks of both octahedra and rods can be indexed to cubic phase CeO_2 (JCPDF 43-1002). The organic-capping-free surface and good dispersion of the CeO_2 nanostructures are the two most critical factors for the subsequent step involving Pt deposition on the surface of CeO_2 via e-beam evaporation.

The detailed shape and crystal facets of the CeO_2 nanostructures were studied by high-resolution transmission electron microscopy (HRTEM). The HRTEM images of octahedral CeO_2 show lattice planes with d-spacing of 0.32 nm corresponding to the (111) planes of cubic CeO_2 (Figs. 3(a) and 3(b)). This suggests that the octahedra were mainly enclosed by (111) facets, which have the highest surface density of atoms and the lowest surface energy for a face-centered cubic structure. Truncated apexes of the CeO_2 octahedra were observed on some of the HRTEM images. The exposed facets of the truncated apexes are (200). Figures 3(c) and 3(d) show typical HRTEM images of

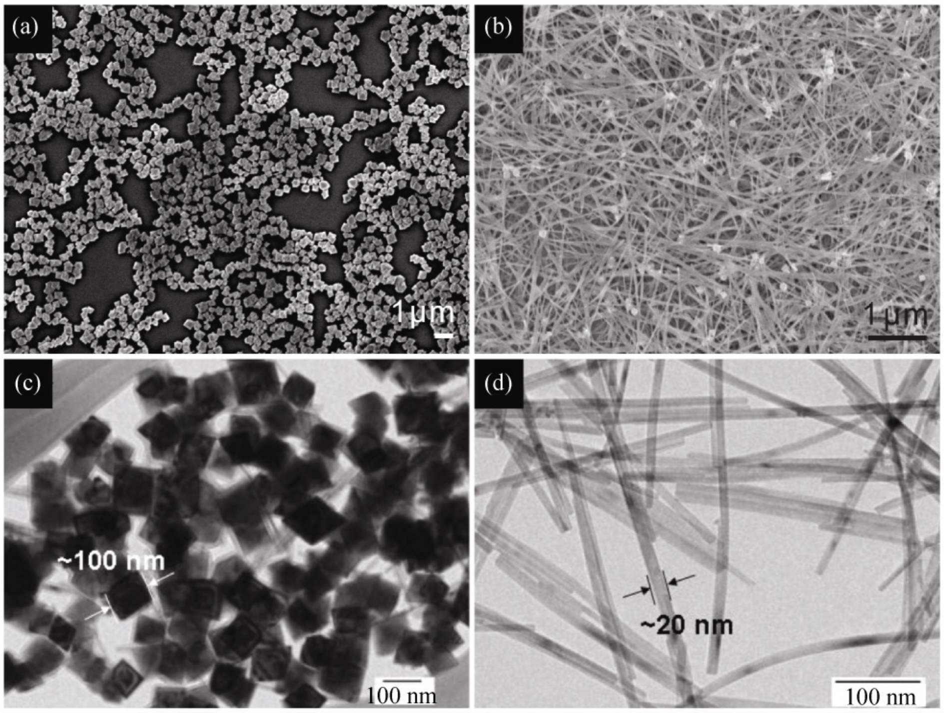

Figure 1 SEM and TEM images of (a) and (c) CeO_2 nanooctahedra (b) and (d) CeO_2 nanorods

the CeO_2 nanorods. The clear lattice images indicate the good crystallinity and single crystalline nature of the CeO_2 nanorods. The interplanar spacings in the HRTEM images suggest that the predominant facets of the CeO_2 nanorods are (200) and (110), rather than the (111) facets found for the nanooctahedra. The nanorods are characterized by rough edges, in contrast to the smooth edges of the nanooctahedra; this represents an additional important difference between the surfaces of the two materials.

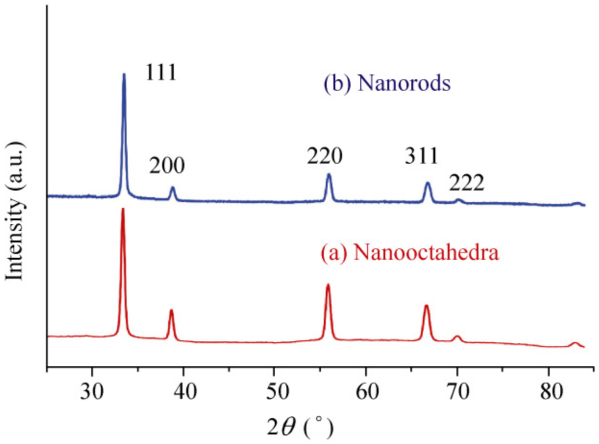

Figure 2 XRD patterns of (a) CeO_2 nanooctahedra. (b) CeO_2 nanorods

As shown in Fig. 4, Ce (3d) XPS of both rod and octahedron-shaped CeO_2 shows characteristic main and satellite peaks due to Ce^{4+} and Ce^{3+} ions. Due to the complexity of the XPS, we followed the deconvolution procedure described by Schierbaum [28] and Kotani [29]. The XPS of Ce^{3+} ($3d_{5/2}$) shows two binding energy peaks at 880 and 885 eV (satellite peak). For Ce^{4+} ($3d_{5/2}$), the XPS shows three binding energy peaks at 882.6, 888.4 (satellite peak), and 898.2 eV (satellite peak). The other five peaks at higher binding energy correspond to the $3d_{3/2}$ states of Ce^{3+} and Ce^{4+} ions with 2/3 of the intensity of the corresponding $3d_{5/2}$ peaks. All peak positions were fixed for the two spectra in order to comparing their relative intensity. It is very clear that the CeO_2 rods contain more Ce^{3+} compared to the octahedral CeO_2. From the deconvoluted peak area, Ce^{3+} ions account for 59.8% of cerium on the surface of CeO_2 rods, while only 28% of cerium on the CeO_2 octahedra is in the Ce^{3+} state.

3.2 Deposition of Pt nanoclusters on CeO_2 nanostructure surface

Silicon wafers and TEM grids with CeO_2 nanorods and nanooctahedra layers were used as the substrates

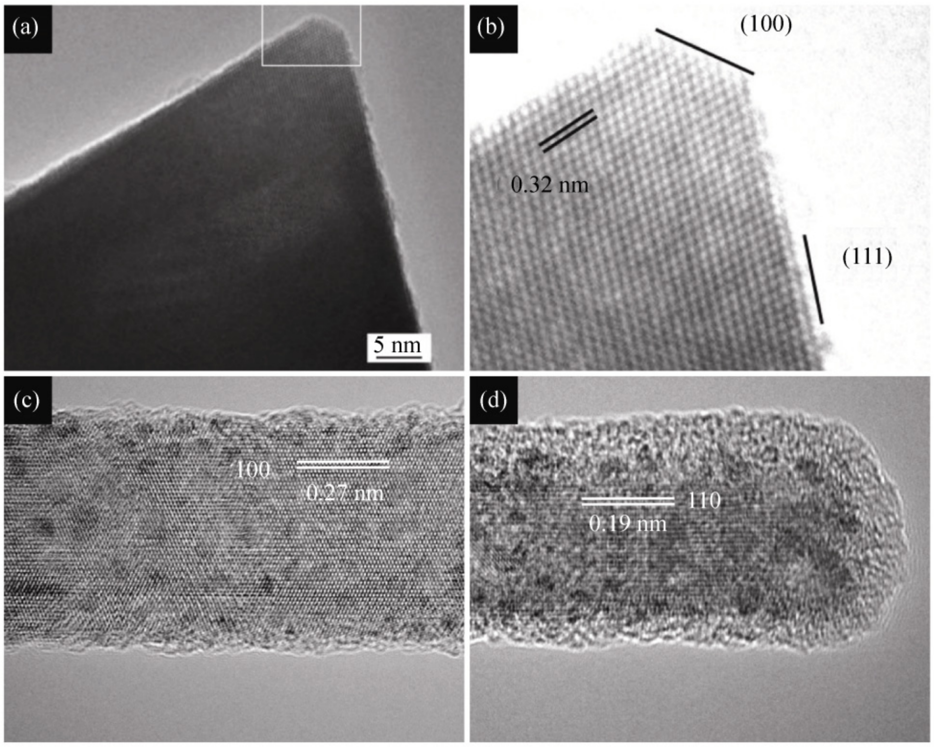

Figure 3 (a) HRTEM image of a CeO_2 nanooctahedron. (b) Shows a magnified view of the selected area of (a). (c) and (d) HRTEM images of CeO_2 nanorods

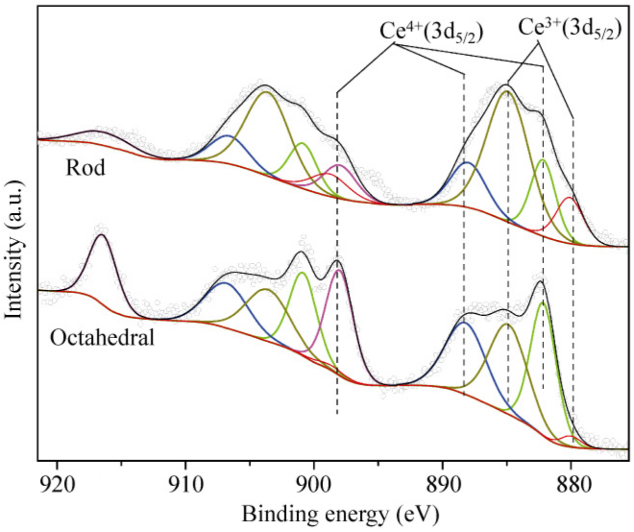

Figure 4 Ce (3d) XPS spectra of CeO_2 nanorods and CeO_2 nanooctahedra

for e-beam Pt evaporation for the purpose of catalysis studies and TEM analyses, respectively. The Pt evaporation rate and deposition amount were monitored by a crystal monitor. The evaporation rate was controlled by the e-beam current and was fixed at 0.01 nm/s. The amount of Pt deposited was controlled by varying the evaporation time. Figures 5(a) and 6(a) show TEM images of Pt cluster layers on CeO_2 nanooctahedra and nanorods, respectively, after an evaporation time of 20 seconds. Pt nanoclusters with a uniform diameter of about 1 nm were distributed evenly on both CeO_2 octahedra and rods. Figures 5(b), 5(c), and 5(d) show HRTEM images of an individual Pt/CeO_2 nanooctahedron. Figure 5(d) and the inset of Fig. 5(b) show magnified views of the selected areas in Figs. 5(c) and 5(b), respectively. These HRTEM images clearly show that most Pt nanoclusters are oriented in the [111] direction on the surface of the CeO_2 nanooctahedron, which is the (111) facet of CeO_2. The magnified views show the great structural homogeneity and high degree of alignment of the (111) zone axis of the Pt nanoclusters. This suggests an epitaxial growth of Pt on the surface of the CeO_2 octahedra. The HRTEM image of CeO_2 nanorods after Pt deposition for 20 seconds is shown in Fig. 6(b). The HRTEM image of Pt deposition on CeO_2 indicates that Pt nanoclusters were oriented in the [111] direction on

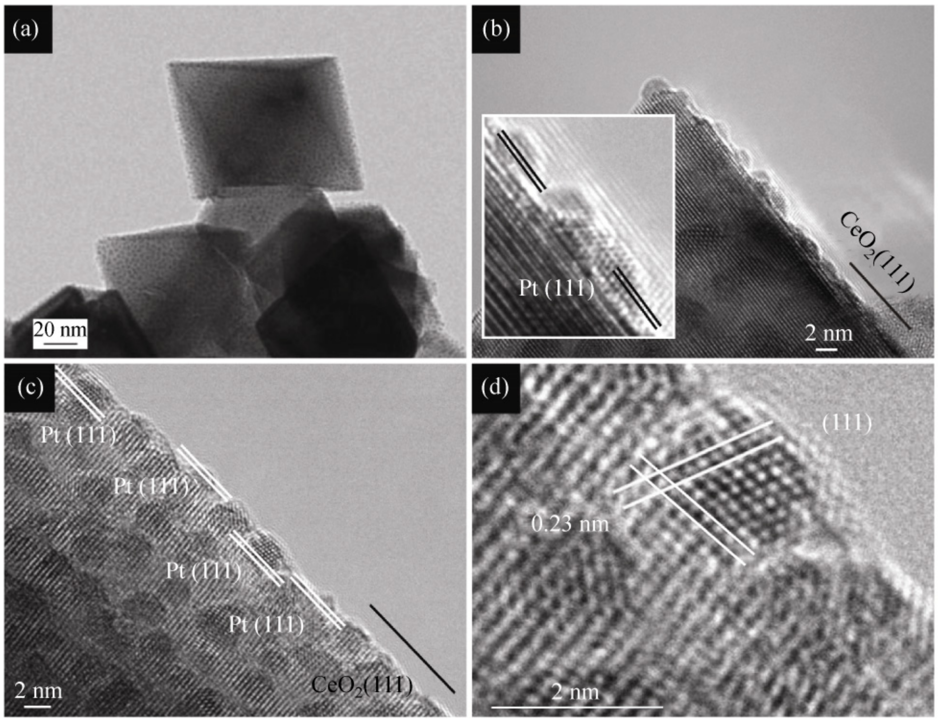

Figure 5 (a) TEM image of CeO_2 nanooctahedra decorated with a Pt nanocluster layer. (b, c) HRTEM images of CeO_2 nanooctahedra decorated with a Pt layer. (d) and the inset in (b) show magnified views of the selected areas in (c) and (b), respectively

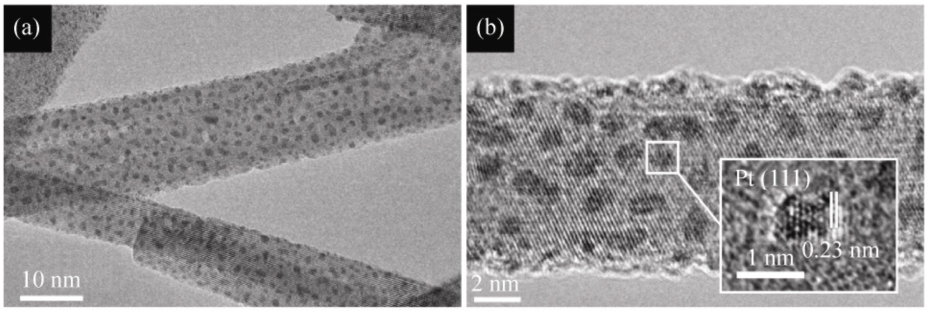

Figure 6 (a) TEM image of CeO_2 nanorods coated with a Pt nanocluster layer and (b) HRTEM images of CeO_2 nanorods coated with a Pt layer. The inset in (b) shows a magnified view of the selected area

the surface of the CeO_2 nanorods. The nanoclusters were slightly smaller than the Pt nanoclusters on found on the nanooctahedra. In order to further investigate the growth of Pt on the CeO_2 rods, longer evaporation times were also employed. HRTEM images (Fig. 7) indicate that most of the resulting 3 nm Pt nanoclusters were also oriented in the [111] direction on the surface of the CeO_2 nanorods. The magnified views indicate the high degree of crystallinity of the Pt nanoclusters but no lattice alignment was observed. It is worth mentioning that the coverage of Pt for the samples with 3 nm Pt was very high. About 40–50% of the CeO_2 surface that was exposed to the evaporation was covered by Pt. However, the coverage of the opposite sides of the nanorods is low due to the shadow effect.

In the case of the nanooctahedron, it is enclosed solely by (111) facets. The relatively smooth (111) facets of the octahedra are indicated by the clear and sharp edges of the octahedra in the TEM images. These large and smooth (111) facets on the octahedra provide ideal substrates for Pt deposition and contribute to the epitaxial growth of Pt nanoclusters. In contrast, CeO_2 nanorods have different exposed surface planes

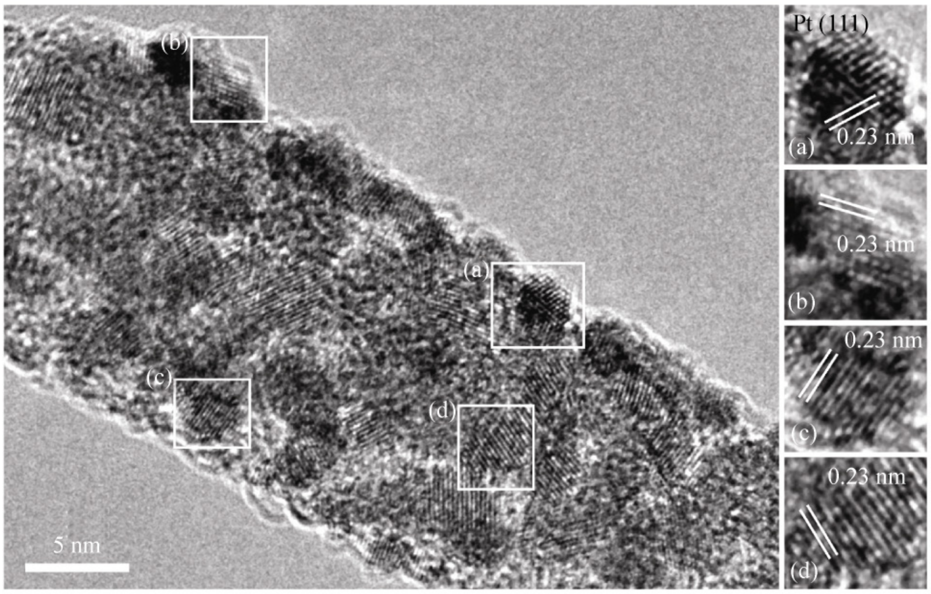

Figure 7 HRTEM image of a CeO_2 nanorod with 3 nm thick Pt deposition

and different Pt cluster growth is observed. Our observations clearly indicate that the structure of the CeO_2 nanocrystals plays an important role in Pt deposition. Different structures of the CeO_2 support result in different growth behaviors of Pt. The different growth behaviors affect the size, structure, and coverage of Pt on CeO_2. All these parameters change the stability, activity, and selectivity of the Pt on CeO_2 catalysts.

3.3 Catalysis

The activities and selectivities of Pt/CeO_2 catalysts for model hydrogenation and oxidation reactions were measured and compared. In order to determine the turnover frequency (TOF), the number of active sites in the Pt catalysts has to be determined first. The number of available Pt sites for reactions is generally determined from H_2 or CO chemisorption measurements [30, 31]. However, for our model catalysts this technique is very challenging, due to the limited amount of metal deposited. It has been demonstrated that ethylene hydrogenation can be used as a chemical probe for estimating the number of available metallic Pt active sites in a catalyst [32]. Ethylene hydrogenation is a classic example of a structure insensitive reaction. The intrinsic catalytic activity is not a function of the Pt surface for this catalytic reaction, which makes it an ideal way to determine the number of available Pt sites. The number of available Pt sites for different Pt/CeO_2 catalysts were calculated and determined by using the TOF of ethylene hydrogenation at 35, 40, 45, 50, and 55 °C, with single crystal and standard Pt catalysts as references. The results are shown in Table 1.

CO oxidation was used as a model reaction to characterize the catalytic properties of Pt/CeO_2 nano-octahedra and nanorods. CeO_2 is an important component in automobile exhaust converters, which is due to its exceptional OSC [33]. During engine operation, CeO_2 adsorbs oxygen from the exhaust under lean conditions (high air-to-fuel ratio) and releases oxygen into the exhaust under rich conditions (low air-to-fuel ratio). CeO_2 undergoes reversible Ce^{4+}/Ce^{3+} redox reactions when it adsorbs or releases oxygen. The superior OSC of CeO_2 maintains the air-to-fuel ratio in the exhaust; this is crucial for ensuring high efficiency of the three-way catalysts in the automobile exhaust converter [34]. The OSC also greatly alters the mechanism of the CO oxidation reaction catalyzed by precious metals supported on CeO_2. In a Pt catalyzed CO oxidation reaction, the oxygen reaction order as well as the reaction activation energy is much lower when CeO_2 is used as the support compared to γ-Al_2O_3 [35]. This indicates that the

Table 1 Catalytic behavior over the Pt/CeO_2 nanostructure catalysts

Catalyst	Available Pt sites (atom)[a]	E_a of ethylene hydrogenation (kcal/mol)[b]	TOF of CO oxidation at 200 °C (s^{-1})[c, e]	E_a of CO oxidation (kcal/mol)[e, f]	TOF of cyclohexene hydrogenation at 120 °C (s^{-1})[d, e]	E_a of cyclohexene hydrogenation (kcal/mol)[e, f]	TOF of cyclohexene dehydrogenation at 150 °C (s^{-1})[d, e]	E_a of cyclohexene dehydrogenation (kcal/mol)[e, f]
Pt/CeO_2 nanooctahedra	6.41×10^{14}	8.87	0.18	34.70	10.23	10.98	4.59	20.13
Pt/CeO nanorods	8.22×10^{14}	7.94	3.10	24.30	10.00	8.52	9.72	25.47

[a] The number of available Pt sites was determined by TOF of ethylene hydrogenation.

[b] Standard conditions were 10 Torr of ethylene and 100 Torr of H_2 with a balance of He.

[c] Standard conditions were 40 Torr of CO and 100 Torr of O_2 and 620 Torr of He.

[d] Standard conditions were 10 Torr C_6H_{10} and 200 Torr of H_2 with a balance of He.

[e] Normalized by the total number of surface atoms determined by ethylene hydrogenation.

[f] The activity in this temperature regime displays "normal" Arrhenius temperature-dependent behavior; 170 °C–230 °C for CO oxidation, 130–160 °C for hydrogenation and 170–200 °C for dehydrogenation.

Pt/CeO_2 catalyst is more active and the reaction is less dependent on the oxygen concentration of the gas phase compared to Pt/ γ-Al_2O_3.

The OSC of CeO_2 depends on the ease of the reversible Ce^{4+}/Ce^{3+} redox cycles, which can be affected by many factors, such as crystal facets, surface roughness, the concentration and distribution of oxygen vacancies, as well as the size of the oxygen vacancy clusters [36–38]. The predominant facets of the CeO_2 nanorods are crystallographically distinct from those of the nanooctahedra. These distinct differences in surface structure should be reflected in the catalytic properties of Pt/CeO_2 nanooctahedra and nanorods in the CO oxidation reaction. Indeed, the Pt/CeO_2 nanorods catalyst was found to be 17 times more active than Pt/CeO_2 nanooctahedra, with TOFs at 200 °C of 3.1 and 0.18 s^{-1}, respectively. The CeO_2 nanorods and nanooctahedra before Pt deposition show no CO conversion under the same reaction conditions. The activation energies for Pt/CeO_2 nanorods and nanooctahedra are 24.3 and 34.7 kcal/mol, respectively. These results are consistent with our XPS study, in which 60 and 28% of cerium exists as Ce^{3+} ions on the surface of CeO_2 nanorods and nanooctahedra, respectively. The high concentration of Ce^{3+} ions on the surface of the CeO_2 nanorods reflects the high concentration of surface oxygen vacancies. Because oxygen diffusion is considered to be the rate controlling step in the CO oxidation reaction on Pt/CeO_2 catalysts [36, 38], the high concentration of oxygen vacancies on CeO_2 nanorods enhances the diffusion of oxygen, and thus, makes the Pt/CeO_2 nanorods more active compared with the Pt/CeO_2 nanooctahedra.

Cyclohexene hydrogenation-dehydrogenation over the Pt/CeO_2 catalysts was used as a model reaction to study the structural differences between the Pt species in the Pt/CeO_2 catalysts. Both hydrogenation and dehydrogenation products (cyclohexane and benzene respectively) are thermodynamically allowed and can be formed over Pt catalysts at the temperatures employed (120–200 °C). It has been demonstrated that the hydrogenation of cyclohexene to cyclohexane is structure insensitive, whereas the dehydrogenation of cyclohexene to benzene is structure sensitive [39–42]. The dehydrogenation of cyclohexene proceeds more rapidly on the Pt(100) crystal surface than on the Pt(111) crystal surface due to the different distributions of reaction intermediates on the Pt surfaces. The activity, TOF, and apparent activation energy for both the hydrogenation and dehydrogenation of cyclohexene are summarized in Table 1. As expected, the hydrogenation TOF at 120 °C was structure insensitive; the rates were around 10 s^{-1} and the activation energies were around 10 $kcal \cdot mol^{-1}$ for both catalysts. This result is in agreement with those for Pt single crystals reported previously. It also confirms that the numbers of available Pt sites determined by ethylene hydrogenation are correct. The kinetics of the dehydrogenation of cyclohexene at 150 °C are also reported in Table 1. The TOF values for dehydrogenation are 4.59 and 9.72 s^{-1} for Pt/CeO_2 nanooctahedra and nanorods, respectively. In other words, the selectivity to benzene over the Pt/CeO_2 nanorods is two times higher than that for the Pt/CeO_2 octahedra. The activation energies are 20.13 and 25.47 kcal·mol^{-1} for Pt/CeO_2 nanooctahedra and nanorods, respectively. Similar structure-dependent selectivities and activation energies have also been observed in studies of Pt single crystals. [43, 44]. Under the same reaction conditions employed in this study, the selectivity to benzene on Pt(111) was higher than on Pt(100) and the activation energy for dehydrogenation on Pt(111) was lower than on Pt (100). Our results are not conclusive enough to determine the dominant crystal facets on the Pt nanocluster, but clearly indicate the structural differences between the epitaxial growth of Pt on CeO_2 nanooctahedra and the random growth of Pt on CeO_2 nanorods.

4. Conclusions

Pt nanocluster layers have been deposited on the surface of capping-agent-free CeO_2 nanooctahedra and nanorods via an e-beam evaporation strategy. The coverage of the Pt nanocluster layer could be controlled by adjusting the e-beam evaporation time. The e-beam evaporated Pt nanocluster layers on CeO_2 surfaces have a clean surface and a clean interface between Pt and CeO_2. Different growth behaviors of Pt on the two CeO_2 nanocrystals were observed. The epitaxial growth of Pt was observed on the CeO_2 octahedra. A high degree of lattice alignment between the Pt clusters on CeO_2 was shown in the HRTEM images of nanooctahedron system, but not in the nanorod system where the growth was random. The structures of the Pt clusters on the two different CeO_2 nanocrystals have been studied and compared by means of model reactions with the catalysts. The results of hydrogenation reactions clearly show the clean and similar chemical surface of Pt clusters in both catalysts. The support-dependent activity of these catalysts is demonstrated by CO oxidation. The Pt/CeO_2 nanorods show much higher activity compared with Pt/CeO_2 nanooctahedra because of the higher concentration of oxygen vacancies in the CeO_2 nanorods. The structure-dependent selectivity of dehydrogenation indicates that the structures of the Pt species on CeO_2 nanorods and nanooctahedra were different, showing how the metal deposition behavior can be modulated by the strong metal–metal oxide interactions.

Acknowledgements

This work was supported by Toyota Motor Engineering and Manufacturing North America (TEMA) Inc. We would like thank Dr. Kimber Stamm for helpful discussion.

References

[1] Narayanan, R.; El-Sayed, M. A. Shape-dependent catalytic activity of platinum nanoparticles in colloidal solution. *Nano Lett.* **2004**, *4*, 1343–1348.

[2] Zhang, Y.; Grass, M. E.; Habas, S. E.; Tao, F.; Zhang, T.; Yang, P.; Somorjai, G. A. One-step polyol synthesis and Langmuir–Blodgett monolayer formation of size-tunable monodisperse rhodium nanocrystals with catalytically active (111) surface structures. *J. Phys. Chem. C* **2007**, *111*, 12243–12253.

[3] Huang, W.; Kuhn, J. N.; Tsung, C. K.; Zhang, Y.; Habas, S. E.; Yang, P.; Somorjai, G. A. Dendrimer templated synthesis of one nanometer Rh and Pt particles supported on mesoporous silica: Catalytic activity for ethylene and pyrrole hydrogenation. *Nano Lett* **2008**, *8*, 2027–2034.

[4] Lim, B.; Jiang, M.; Camargo, P. H. C.; Cho, E. C.; Tao, J.; Lu, X.; Zhu, Y.; Xia, Y. Pd–Pt bimetallic nanodendrites with high activity for oxygen reduction. *Science* **2009**, *324*, 1302–1305.

[5] Diebold, U. The surface science of titanium dioxide. *Surf. Sci. Rep.* **2003**, *48*, 53–229.

[6] Haruta, M.; Date, M. Advances in the catalysis of Au nanoparticles. *Appl. Catal. A–Gen.* **2001**, *222*, 427–437.

[7] Banares, M. A. Supported metal oxide and other catalysts for ethane conversion: A review. *Catal. Today* **1999**, *51*, 319–348.

[8] Stakheev, A. Y.; Kustov, L. M. Effects of the support on the morphology and electronic properties of supported metal clusters: Modern concepts and progress in 1990s. *Appl. Catal. A–Gen.* **1999**, *188*, 3–35.

[9] Bratlie, K. M.; Lee, H.; Komvopoulos, K.; Yang, P.; Somorjai, G. A. Platinum nanoparticle shape effects on benzene hydrogenation selectivity. *Nano Lett.* **2007**, *7*, 3097–4101.

[10] Lee, H.; Habas, S. E.; Kweskin, S.; Butcher, D.; Somorjai, G. A.; Yang, P. Morphological control of catalytically active platinum nanocrystals. *Angew. Chem. Int. Ed.* **2006**, *45*, 7824–7828.

[11] Peng, Z. M.; Yang, H. Paleostructural geomorphology of the Paleozoic central uplift belt and its constraint on the development of depositional facies in the Tarim Basin. *J. Am. Chem. Soc.* **2009**, *131*, 7542–7543.

[12] Okumura, M.; Nakamura, S.; Tsubota, S.; Nakamura, T.; Azuma, M.; Haruta, M. Chemical vapor deposition of gold on Al_2O_3, SiO_2, and TiO_2 for the oxidation of CO and of H_2. *Catal. Lett.* **1998**, *51*, 53–58.

[13] Kakuta, N.; Morishima, N.; Kotobuki, M.; Iwase, T.; Mizushima, T.; Sato, Y.; Matsuura, S. Oxygen storage capacity (OSC) of aged $Pt/CeO_2/Al_2O_3$ catalysts: Roles of Pt and CeO_2 supported on Al_2O_3. *Appl. Surf. Sci.* **1997**, *121/122*, 408–412.

[14] Dutta, P.; Pal, S.; Seehra, M. S.; Shi, Y.; Eyring, E. M.; Ernst, R. D. Concentration of Ce^{3+} and oxygen vacancies in cerium oxide nanoparticles. *Chem. Mater.* **2006**, *18*, 5144–5146.

[15] Schubert, M. M.; Plzak, V.; Garche, J.; Behm, R. CO oxidation over supported gold catalysts-“inert” and “active” support materials and their role for the oxygen supply during reaction. *J. Catal. Lett.* **2001**, *76*, 143–150.

[16] Mai, H. X.; Sun, L. D.; Zhang, Y. W.; Si, R.; Feng, W.; Zhang, H. P.; Liu, H. C.; Yan, C. H. Shape-selective synthesis and oxygen storage behavior of ceria nanopolyhedra, nanorods, and nanocubes, *J. Phys. Chem. B* **2005**, *109*, 24380–24385.

[17] Sun, C.; Sun, J.; Xiao, G.; Zhang, H.; Qiu, X.; Li, H.; Chen, L. Mesoscale organization of nearly monodisperse flowerlike ceria microspheres. *J. Phys. Chem. B* **2006**, *110*, 13445–13452.

[18] Chen, G.; Xu, C.; Song, X.; Zhao, W.; Ding, Y.; Sun, S. Interface reaction route to two different kinds of CeO_2 nanotubes. *Inorg. Chem.* **2008**, *47*, 723–728.

[19] Bernal, S.; Calvino, J. J.; Cauqui, M. A.; Gatica, J. M.; Larese, C.; Omil, J. A. P.; Pintado, J. M. Some recent results on metal/support interaction effects in NM/CeO_2 (NM: noble metal) catalysts. *Catal. Today* **1999**, *50*, 175–206.

[20] Guzman, J.; Carrettin, S.; Corma, A. Spectroscopic evidence for the supply of reactive oxygen during CO oxidation catalyzed by gold supported on nanocrystalline CeO_2. *J. Am. Chem. Soc.* **2005**, *127*, 3286–3287.

[21] Huang, P. X.; Wu, F.; Zhu, B. L.; Gao, X. P.; Zhu, H. Y.; Yan, T. Y.; Huang, W. P.; Wu, S. H.; Song, D. Y. CeO_2 nanorods and gold nanocrystals supported on CeO_2 nanorods as catalyst. *J. Phys. Chem. B* **2005**, *109*, 19169–19174.

[22] Hickey, N.; Larochette, P. A.; Gentilini, C.; Sordelli, L.; Olivi, L.; Polizzi, S.; Montini, T.; Fornasiero, P.; Pasquato, L.; Graziani, M. Monolayer protected gold nanoparticles on ceria for an efficient CO oxidation catalyst. *Chem. Mater.* **2007**, *19*, 650–651.

[23] Wei, J. M.; Iglesia, E. Mechanism and site requirements for activation and chemical conversion of methane on supported Pt clusters and turnover rate comparisons among noble metals. *J. Phys. Chem. B* **2004**, *108*, 4094–4103.

[24] Jacobs, G.; Graham, U. M.; Chenu, E.; Patterson, P. M.; Dozier, A.; Davis, B. H. Low-temperature water–gas shift: Impact of Pt promoter loading on the partial reduction of ceria and consequences for catalyst design. *J. Catal.* **2005**, *229*, 499–512.

[25] Ferreira, A. P.; Zanchet, D.; Araujo, J. C. S.; Liberatori, J. W. C.; Souza-Aguiar, E. F.; Noronha, F. B.; Bueno, J. M. C. The effects of CeO_2 on the activity and stability of Pt supported catalysts for methane reforming, as addressed by *in situ* temperature resolved XAFS and TEM analysis. *J. Catal.* **2009**, *263*, 335–344.

[26] Si, R.; Flytzani-Stephanopoulos, M. Shape and crystal-plane effects of nanoscale ceria on the activity of $Au–CeO_2$ catalysts for the water–gas shift reaction. *Angew. Chem. Int. Ed.* **2008**, *47*, 2884–2887.

[27] Yan, L.; Yu, R.; Chen, J.; Xing, X. Template-free hydrothermal synthesis of CeO_2 nano-octahedrons and nanorods: Investigation of the inorphology evolution. *Cryst. Growth Des.* **2008**, *8*, 1474–1477.

[28] Schierbaum, K. D. Controlled synthesis of CeO_2 flower-like and well-aligned nanorod hierarchical architectures by a phosphate-assisted hydrothermal route. *Surf. Sci.* **1998**, *399*, 29–38.

[29] Kotani, A.; Ogasawara, H. Theory of core-level spectroscopy of rare-earth oxides. *J. Electron Spectrosc. Rel. Phenom.* **1992**, *60*, 257–299.

[30] Tsung, C. K.; Kuhn, J. N.; Huang, W. Y.; Aliaga, C.; Hung, L. I.; Somorjai, G. A.; Yang, P. D. Sub-10 nm platinum nanocrystals with size and shape control: Catalytic study for ethylene and pyrrole hydrogenation. *J. Am. Chem. Soc.* **2009**, *131*, 5816–5822.

[31] Song, H.; Rioux, R. M.; Hoefelmeyer, J. D.; Komor, R.; Niesz, K.; Grass, M.; Yang, P. D.; Somorjai, G. A. Hydrothermal growth of mesoporous SBA-15 silica in the presence of PVP-stabilized Pt nanoparticles: Synthesis, characterization, and catalytic properties. *J. Am. Chem. Soc.*

2006, *128*, 3027–3037.

[32] Kuhn, J. N.; Tsung, C. K.; Huang, W.; Somorjai, G. A. Effect of organic capping layers over monodisperse platinum nanoparticles upon activity for ethylene hydrogenation and carbon monoxide oxidation. *J. Catal.* **2009**, *265*, 209–215.

[33] Trovarelli, A. Catalytic properties of ceria and CeO_2-containing materials. *Catal. Rev.–Sci. Eng.* **1996**, *38*, 439– 520.

[34] Kaspar, J.; Fornasiero, P.; Hickey, N. Automotive catalytic converters: Current status and some perspectives. *Catal. Today* **2003**, *77*, 419–449.

[35] Oran, U.; Uner, D. Mechanisms of CO oxidation reaction and effect of chlorine ions on the CO oxidation reaction over Pt/CeO_2 and Pt/CeO_2/gamma-Al_2O_3 catalysts. *Appl. Catal. B–Environ.* **2004**, *54*, 183–191.

[36] Esch, F.; Fabris, S.; Zhou, L.; Montini, T.; Africh, C.; Fornasiero, P.; Comelli, G.; Rosei, R. Electron localization determines defect formation on ceria substrates. *Science* **2005**, *309*, 752–755.

[37] Sayle, T. X. T.; Parker, S. C.; Catlow, C. R. A. The role of oxygen vacancies on ceria surfaces in the oxidation of carbon monoxide. *Surf. Sci.* **1994**, *316*, 329–336.

[38] Liu, X. W.; Zhou, K. B.; Wang, L.; Wang, B. Y.; Li, Y. D. Oxygen vacancy clusters promoting reducibility and activity of ceria nanorods. *J. Am. Chem. Soc.* **2009**, *131*, 3140–3141.

[39] Segal, E.; Madon, R. J.; Boudart, M. The structure and activity of supported metal catalysts: I. Crystallite size and specific activity for benzene hydrogenation of platinum/silica catalysts. *J. Catal.* **1978**, *52*, 45–49.

[40] Dorling, T. A.; Moss, R. L. The structure and activity of supported metal catalysts: I. Crystallite size and specific activity for benzene hydrogenation of platinum/silica catalysts. *J. Catal.* **1966**, *5*, 111–115.

[41] Davis, S. M.; Somorjai, G. A. Correlation of cyclohexene reactions on platinum crystal surfaces over a ten-order-of-magnitude pressure range: Variations of structure sensitivity, rates, and reaction probabilities. *J. Catal.* **1980**, *65*, 78–83.

[42] McCrea, K. R.; Somorjai, G. A. SFG-surface vibrational spectroscopy studies of structure sensitivity and insensitivity in catalytic reactions: Cyclohexene dehydrogenation and ethylene hydrogenation on Pt(111) and Pt(100) crystal surfaces. *J. Mol. Catal. A–Chem.* **2000**, *163*, 43–53.

[43] Yang, M. C.; Rioux, R. M.; Somorjai, G. A. Reaction kinetics and *in situ* sum frequency generation surface vibrational spectroscopy studies of cycloalkene hydrogenation/dehydrogenation on Pt(111): Substituent effects and CO poisoning. *J. Catal.* **2006**, *237*, 255–266.

[44] Bratlie, K. M.; Flores, L. D.; Somorjai, G. A. Hydrogenation and dehydrogenation of cyclohexene on Pt(100): A sum frequency generation vibrational spectroscopic and kinetic study. *Surf. Sci.* **2005**, *599*, 93–106.